Research Paper

Evidence of phyllosilicate alteration processes and clay mineral neoformation promoted by hydrothermal fluids in the Padul Fault area (Betic Cordillera, SE Spain)

Isabel Abad [a],[*], Fernando Nieto [b], Matías Reolid [a], Juan Jiménez-Millán [a]

[a] *Departamento de Geología y CEACTEMA, Unidad Asociada IACT, Universidad de Jaén, Campus Las Lagunillas, 23071 Jaén, Spain*
[b] *Departamento de Mineralogía y Petrología e IACT, Universidad de Granada-CSIC, Fuentenueva s/n, 18002 Granada, Spain*

A B S T R A C T

Geochemical changes and authigenic clays were detected in the fault rocks of the Padul Fault. An enrichment from the protolith to the ultracataclasites in Si, Al, Fe, Ca, Ti and also Zn but an impoverishment in Mg was detected. Although the protolith (dolostones) and fault rocks are mostly composed of carbonates, the fault rocks are also characterized by the presence of fine-grained clays in the matrix (mainly chlorite and Mg-rich biotite, but also smectite and punctually talc). Neither chlorite nor talc were detected in the protolith. The application of chlorite thermometry gives temperatures around 140–220 °C for chlorites lamellae located on the fault plane. These chlorites are compositionally homogeneous, whereas the chlorites detected in the cataclasites are more variable, although both of them are Mg-rich and have almost no Fe. As well, chlorites from the cataclasites usually include Zn in their composition and, as observed at nanoscale, they are genetically related to biotites, which come from the protolith. Talc grains (< 1 μm) are always found between dolomite and calcite. These observations point to clay mineral reactions in the fault rocks as the chlorite and talc precipitation promoted by circulation of fault-controlled hydrothermal fluids close to 200 °C. Other clays such as smectite are the result of the final step of the hydrothermal activity in the fault. The identification of authigenic clay minerals, which cause weakening mechanisms, is consistent with the geodetic characterization of the Padul Fault, which plays an important role in aseismic deformation.

1. Introduction

The southern Iberian Peninsula is a tectonically active area as a consequence of the convergence of the Eurasian and the African plates. A main feature of this geotectonic context is the existence of many active faults such as those located in the Granada Basin, in the central sector of the Betic Cordillera. Here, the extension is accomodated by normal faults with a predominantly NW-SE strike. One of them is the Padul Fault, in the southeastern part of the Granada Basin (Fig. 1). Whereas there is abundant structural fieldwork research developed in this location (Alfaro et al., 2001; Galindo-Zaldívar et al., 2003; Gil et al., 2017; among others), less attention has been given to mineralogical/geochemical characterization as potential features that can modify the rheology during fault zone evolution. Jiménez-Millán et al. (2015) and Abad et al. (2017, 2019) evidenced that the mineralogy is probably a primary control on deformation as proposed previously by other authors

(e.g., Kristensen et al., 2013). Mechanical and hydrological properties of crustal faults are conditioned by lithological variations. The occurrence of phyllosilicates or other weak minerals (clays, anhydrite) in a fault zone can promote distributed deformation and provide a potential explanation for fault weakness (Faulkner et al., 2003; Buatier et al., 2012; Tesei et al., 2014; Smeraglia et al., 2017; among others).

The textural and mineralogical characterizations up to the nanoscale and the analysis of the major and trace elements in the samples (fault rocks and the protolith) aim to determine the low-temperature processes that affected to these materials during the development of the extensional fault zone. Attention has been paid to clay minerals as they are known to have a crucial role on the fault behaviors (e.g., Van der Pluijm, 2011; Jiménez-Millán et al., 2015; Smeraglia et al., 2017; among others). But this is not an easy task often due to the fine-grain size and poor crystallinity of these mineral phases, which has implied the use of transmission electron microscopy for a detailed study in selected
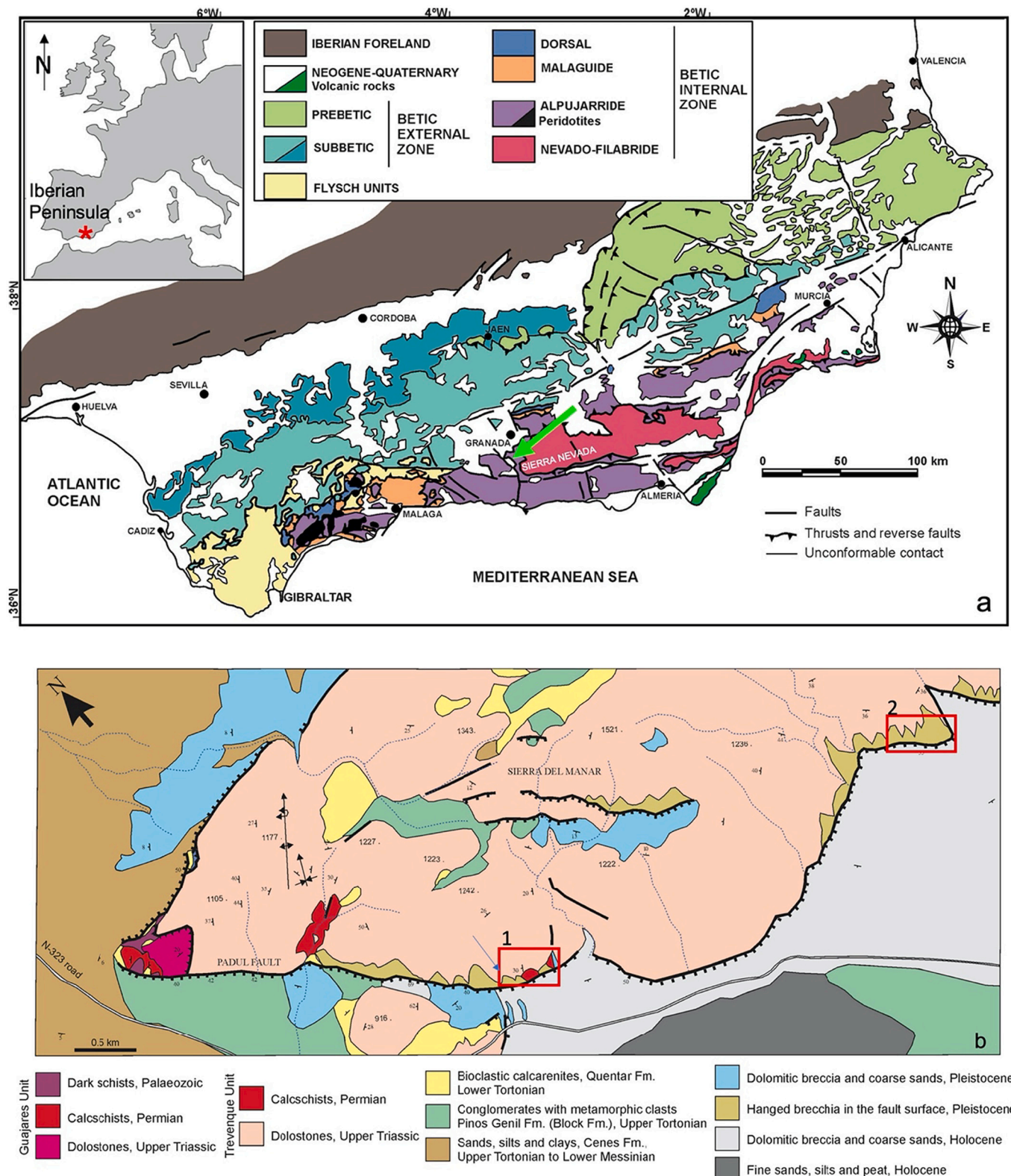
Fig. 1. (a) Geological context of the study area with indication of the location of the Padul fault (green arrow) in the Internal Zone (Alpujárride Complex) of the Betic Cordillera (modified from Fig. 3 in Sanz de Galdeano, 2022). (b) Detailed geological map of the Padul Fault in the south of the Granada basin with approximated indication of the studied outcrops (red rectangles, 1: Motrilejo quarries; 2: Marchena zone). (For interpretation of the references to colour in this figure legend, the reader is referred to the web version of this article.)

samples providing a significant and relevant amount of data. This is a study involving interpretation of exhumed fault rocks. However, while outcrops provide natural laboratories at much larger observational scale than a drill core, some parameters as depth, temperature and geological setting during deformation must be interpreted. The sample collection has been focused on the fault core that is in the zone characterized by the slip surface, which is mainly composed of ultracataclasites and cataclasites.

In the studied case, we combined mineralogical and geochemical methods (X-ray diffraction, optical and - scanning and transmission - electron microscopy, electron microprobe and whole rock geochemistry) to determine the fault-rock chemistry, mineralogy and microtextures which allowed us to provide mechanisms of clay formation and to speculate about the Padul Fault behavior.

2. Geological setting and materials

The Betic Cordillera (southern Spain) is the westernmost European Alpine chain. This ENE–WSW-trending fold-and thrust belt is composed of the External Zone and the Internal Zone (Fig. 1a). The External Zone is characterized by Mesozoic to Tertiary rocks corresponding to the Iberian Plate palaeomargin, situated on top of the Variscan basement. The Internal Zone corresponds to the Alborán Domain and consists of a thrust stack of metamorphic complexes (Nevado-Filábride, Alpujárride and Maláguide) affected by major tectonism and large displacements during the early Miocene (e.g., Aldaya et al., 1979; Sanz de Galdeano, 1990; Azañón and Crespo-Blanc, 2000; Sanz de Galdeano and López-Garrido, 2003; Sanz de Galdeano et al., 2019). Superimposed on these structures are Neogene to Quaternary sediments filling the intramountain basins, limited by E–W and NE–SW faults (Montenat and Ott D'Estevou, 1995; Galindo Zaldívar et al., 1999).

2.1. The Padul Fault

The Padul Fault, which is also known as the Padul-Nigüelas Fault, is the most remarkable normal fault from the central sector of the Betic Cordillera from the geomorphic point of view (e.g., Sanz de Galdeano, 1976; Sanz de Galdeano et al., 1984; Galindo-Zaldívar et al., 2003; Hürtgen et al., 2013). This fault, in the Internal Zone of the cordillera, separates the highest reliefs of Sierra Nevada (footwall block) from the Padul graben at the southeastern border of the Granada Basin (e.g., Sanz de Galdeano, 1976; Sanz de Galdeano and Alfaro, 2004) resulting in a spectacular mountain front, the Sierra del Manar, constituted by carbonate rocks of the Alpujárride Complex.

The fault trends NW-SE with a variable dip to the SW ranging from 60°-65° to <20° and is composed of a northwestern segment of 5.25 km (close to Padul village) and a southeastern segment of 7 km (close to Dúrcal and Nigüelas villages) connected by a 1.5 km relay fault. The throw of the fault is >800 m in its central part (Santanach et al., 1980; Sanz de Galdeano and López-Garrido, 1999) and although the displacements are mainly normal, there is a slight to moderate left lateral component (Gil et al., 2017).

2.2. The Sierra del Manar rocks

The study outcrops are located in the footwall block of the Padul Fault, corresponding to the Sierra del Manar, relief composed mainly of rocks of the Alpujárride Complex (Fig. 1b). The stratigraphic succession of the Alpujárride Complex is constituted by a basement of Paleozoic micaschists and quartzites, and a cover made up by a lower phyllite and quartzite formation of Permian - Anisian, a thick Middle-Upper Triassic carbonate formation, and locally thin Jurassic rocks (Delgado et al., 1981; Braga and Martín, 1987; Sanz de Galdeano and López-Garrido, 2014). Different tectonic units of the Alpujárride Complex are superimposed on the Alpine Orogeny resulting in nappes with distinct metamorphic grade and dolomitization degree (Azañón and Goffé,

1997; Sanz de Galdeano and López-Garrido, 1999, 2014; Azañón and Crespo-Blanc, 2000; Sanz de Galdeano et al., 2019). The Sierra del Manar is composed mainly of dolostones and secondarily metapelitic rocks of the Alpujárride Complex, but also upper Tortonian bioclastic limestones (Quéntar Formation), conglomerates and sands (Pinos Genil Formation or Block Formation) and Messinian marls (Cenes Formation) located at >1300 m elevation.

In the study area, the hanging wall block is located in the Padul graben, which began to form in the Pliocene. The Padul graben was filled mainly by alluvial fans and peat deposits, which were affected by the fault activity during the Pliocene and the Quaternary. As a consequence of this, some fossil alluvial fans are now found at >1200 m high in south face of the Sierra del Manar. Fission track analyses confirm that Sierra Nevada underwent a fast uplift during the Pliocene (Johnson, 1997).

The Sierra del Manar is mainly constituted by the Triassic dolostones of the Alpujárride Complex, which are known as Trevenque Unit (Sanz de Galdeano and López-Garrido, 1999, 2003) and which are affected by low-grade metamorphism. However, in some areas the base of the carbonate formation of the Trevenque Unit is composed of calc-schists. Some small outcrops correspond to Paleozoic dark schists, calc-schists and dolostones of the Guindalera klippes (Aldaya et al., 1979). These rocks are recorded in the northwest end of the Sierra del Manar relief and correspond to the Guajares Unit (Simancas and Campos, 1993; Azañón et al., 1994; Alonso-Chaves and Orozco, 1998; Sanz de Galdeano and López-Garrido, 2003), which overthrusts the Trevenque Unit (Sanz de Galdeano, 1990).

For this study, fault rocks and their respective protoliths were collected from Motrilejo quarries and Marchena zone (Fig. 1b). In the Motrilejo quarries, two outcrops were sampled: (i) ultracataclasites and cataclasites formed from Triassic dolostones taken directly from the fault plane and (ii) a cross-section composed of carbonate rocks where samples were collected from >30 m to the fault plane. Quarrying for three decades removed a major part of the hanging wall colluvium revealing smooth fault planes of >40 m height (Fig. 2a). In the Marchena zone, fault rocks were collected along two ravines with an appearance very similar to the ultracataclasites from the Motrilejo quarries.

3. Methodology

X-ray diffraction (XRD) data were obtained from unoriented powders and oriented aggregates prepared by sedimentation on glass slides (whole-rock samples and, in some specific cases, <2 μm fraction) after washing with distilled water to remove salts. Oriented aggregates were prepared by sedimentation on glass slides and the <2 μm fraction was separated by centrifugation. Ethylene glycol treatment was carried out to permit the identification of expandable minerals.

X-ray diffractograms were obtained in a PANalytical Empyrean diffractometer (CuKα radiation, 45 kV, 40 mA) equipped with an X'Celerator solid-state linear detector and θ/θ goniometer using a virtual step increment of 0.01° 2θ and a counting time of 10 s/step at the Centro de Instrumentación Científico-Técnica (CICT) of the Universidad de Jaén. Dry samples were scanned from 4° to 64° 2θ, while for the glycolated samples the scan was done between 4° and 32° 2θ.

Following the XRD characterization and the examination under magnifying glass and optical microscope at various magnifications of all thin-sections, carbon-coated polished thin sections were examined by Scanning Electron Microscopy (SEM), using back-scattered electron (BSE) imaging in atomic number contrast mode and energy-dispersive X-ray (EDX) analysis to obtain textural and chemical data. Small rock-chips were cut and glued on a sample holder for the morphological characterization of the fault plane using secondary electron imaging. These observations were carried out with a Merlin Carl Zeiss Gemini II SEM with 0.8 nm of resolution and five detectors (one in lens detector for high resolution) at the CICT (Universidad de Jaén). Electron microprobe (EPMA) analyses of phyllosilicates were obtained using
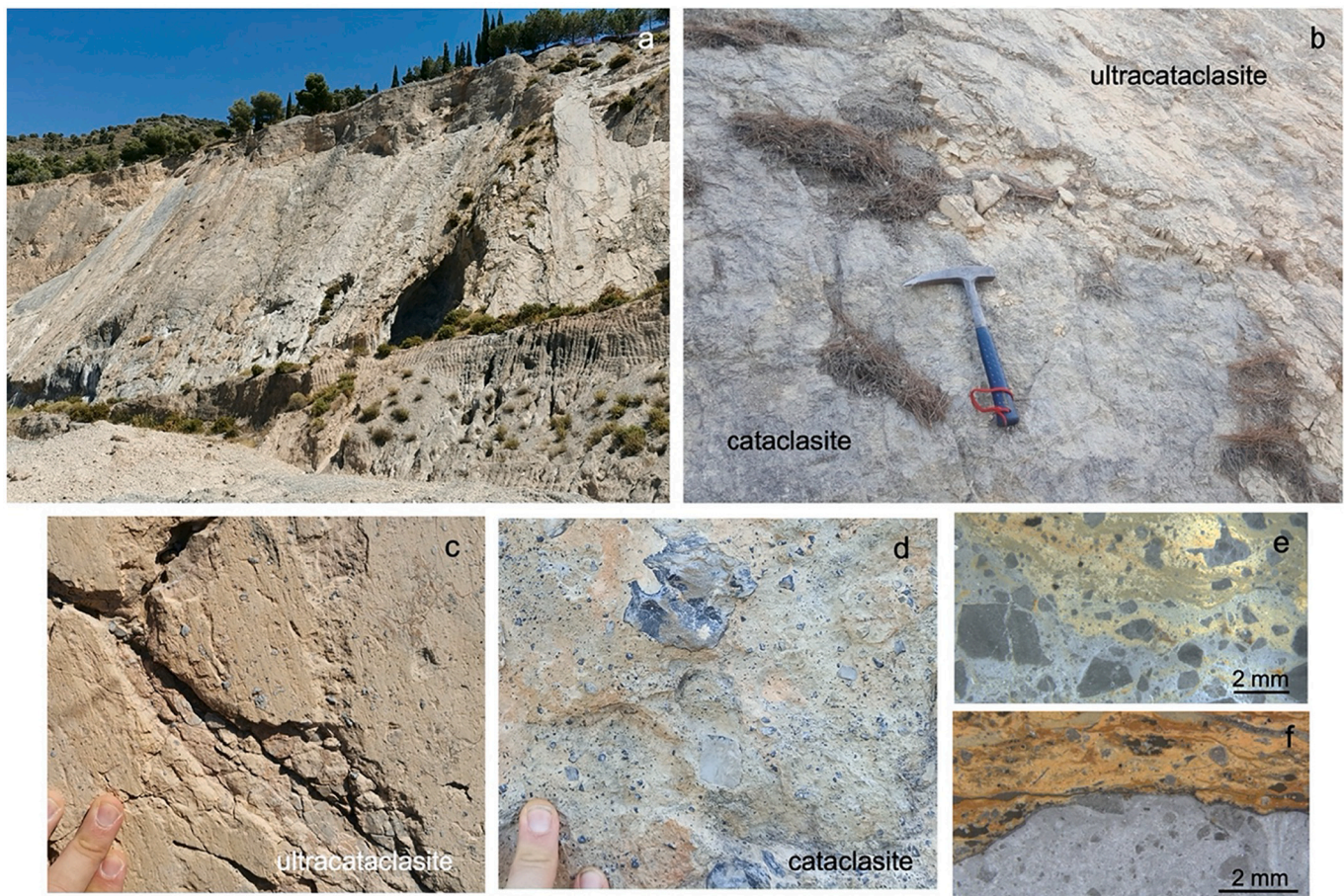
Fig. 2. (a) View of the Motrilejo quarry and the fault plane in the background, dipping around 60° to the SW; (b) fault plane with the two types of fault rocks, cataclasites and ultracataclasites; c-d) aspect of both types of fault rocks; e-f) magnifying glass images of the contact between cataclasites (grey part) and the yellowish ultracataclasites (fault plane upwards).

wavelength-dispersive spectroscopy (WDS) on a Cameca SX100 at the Centro de Instrumentación Científica (CIC) of the Universidad de Granada. The instrument was set at an accelerating voltage of 15 kV, with a beam current of 15 nA and an electron beam diameter of <5 μm. Data were reduced using the procedure of Pouchou and Pichoir (1985) and the standards used were albite, sanidine, periclase, diopside, quartz, vanadinite, rutile, fluorite and synthetic oxides (Al_2O_3, Fe_2O_3, NiO and $MnTiO_3$). Specifically, the chlorite analyses from the fault plane were done on a polished preparation previously impregnated under vacuum with a polyester resin.

Selected samples were prepared as ion-milled specimens for their study by TEM and HRTEM, scanning transmission electron microscopy (STEM) with high-angle annular dark field (HAADF) at the CIC (Universidad de Granada). The copper rings were attached to selected areas of thin sections prepared with Canada balsam. These areas were detached through gentle heating, ion-thinned using a Fischione-1010 ion mill and further carbon coated. The TEM-HRTEM study was conducted through a HAADF Thermo Fisher Scientific TALOS F200X microscope, operating at 200 kV and with a point-to-point resolution of 0.12 nm in the TEM mode and 0.19 nm in the STEM mode. The quantitative micro-to nano-chemical analyses, in STEM mode, were obtained by means of the AEM-EDX (energy dispersive X-ray microscopy), using the Super-X system.

Whole-rock analyses of the major elements of selected samples from the host rocks and fault rocks to compare the variation of chemical composition in different samples were carried out using a PANalytical wavelength dispersive X-ray fluorescence (XRF) spectrometer model Zetium with a maximum power of 4 kW, and provided with a X-ray tube

of Rh anode. Samples were prepared as beads with a Philips Pearlx3. Trace elements were analysed in the same samples using a NexION 300D inductively coupled plasma-mass spectrometer (ICP-MS) after HNO_3 + HF digestion of 100 mg of sample powder in a Teflon-lined vessel at 180 °C and 200 p.s.i. during 30 min, evaporation to dryness, and subsequent dissolution in 100 ml of 4 vol% HNO_3 (both techniques in the CIC, Universidad de Granada). Elemental mappings of fault rocks have been obtained by X ray-microfluorescence M4 Tornado Brucker at the CICT (University of Jaén).

Semi-empirical thermometric methods (Bourdelle et al., 2013; Inoue et al., 2018) were applied in chlorites analysed by EPMA under the conditions previously indicated via the spreadsheet from Verdecchia et al. (2019). The final choice of these two chlorite thermometers was guided by the compositional range of the studied chlorites, and by the temperature range. In both cases, the structural site location of Ti, Mn, Na, Ca, and K was done considering the configuration followed by each author. In addition, Fe, which is present in very small quantities here (<0.05 atoms per formula unit, apfu hereafter), was considered as Fe^{2+}. The uncertainties on the temperature calculations are approximately ±50 °C.

4. Results

4.1. Petrographic characterization

In the fault plane two different types of rocks were sampled: the yellowish ultracataclasites, forming discontinuous patches, probably due to fault scarp erosion, up to 8–10 cm thick resting above the

underlying grey cataclasites (Fig. 2b). The main difference between the yellow ultracataclasites and the grey cataclasites is the abundance and size of the dolomite clasts (Fig. 2c-d). The ultracataclasites with heterometric texture, exhibit dolomite in form of angular clasts of <1 cm of diameter and abundance around 5–10% dispersed within a ground mass composed by very-fine grained material. Nevertheless, the cataclasites show a much higher presence of angular dolomite clasts (around 45%) with sizes up to several centimeters. In both cases the mechanical crushing of the protolith is evident but in any case, the ultracataclasites show more intense grain comminution than the cataclasites. In the fault plane, the boundary between both rocks is clear; under the magnifying glass there is usually a gradual transition sometimes marked by undulations that are visible thanks to the reddish and yellowish colors of the ultrafine-grained matrix that characterizes the ultracataclasites (Fig. 2e) although net limits can also be observed (Fig. 2f).

With respect to the mineralogy, the ultracataclasites are composed not only by carbonates, dolomite and subordinated calcite with sharp chemical boundaries, but also by a little proportion of fine-grained silicates in the matrix: quartz, chlorite and micas in addition to Fe and Ti-oxides and apatite. The SEM characterization of the ultracataclasites shows that there are mainly two micas: Mg-rich biotite and muscovite (Fig. 3a). As well, in some cases, it was possible to observe domains rich in silicates including also paragonite and epidote (Fig. 3b).

The cataclasites matrix shows a mineralogical composition very similar to the ultracataclasites, although the amount of calcite is lower and only in some cases quartz and micas were detected in the X-ray diffractometer. BSE images display the presence of minor chlorite and biotite laths among the predominantly angular dolomite crystals frequently affected by an inner crackle breccia texture, some calcite, Fe and Ti oxides and apatite. The bigger chlorite grains (30–60 μm) show different grey tones in the BSE images (Fig. 3c) and exhibit a variable content of Zn, the same as the biotites (Fig. 3d). Occasionally, talc has been identified in some fault rocks at the micrometer scale, as thin laths of <100 μm long (Fig. 3e). Only in one case, in a cataclasite that appeared to be composed only of carbonates, talc was detected by XRD

(<2 μm fraction) and later confirmed by TEM.

The dolostones (protolith) are composed mainly of dolomite, as well as minor quartz and micas (biotite and muscovite) (Fig. 3f). These biotites are Mg rich and show no Zn at all. It was also observed the occurrence of authigenic smectite/kaolinite filling the interstices among dolomite grains, the smectite aggregates with beidellitic composition. Nevertheless, neither chlorite nor talc were detected in the protolith.

The SE images corresponding to small rock-chips cut from the fault plane allowed to detect the presence of chlorite and minor smectite and biotite grains parallel to the fault plane at the micrometer scale and arranged on rhombohedral dolomite crystals (Fig. 4a-b). These lamellae are responsible of the smooth appearance of the fault plane in some locations. In these clays, Zn is absent (Fig. 4c-e).

4.2. Chemical bulk composition

The XRF data corresponding to major elements of the protolith, cataclasites and ultracataclasites point to an increase in SiO_2 and other oxides (Al_2O_3, Fe_2O_3, and CaO) mainly with a decreasing in MgO from the protolith to the fault plane that contains the ultracataclasites (Fig. 5a-d). In the case of SiO_2, the content is <1 wt% in the protolith, a bit higher than 1 wt% in cataclasites and around 4–5 wt% in ultracataclasites. Al_2O_3 and Fe_2O_3 contents increase from nil to 3 wt% (Al) and 1 wt% (Fe) in the fault rocks. CaO undergoes however a more relevant increase from ~30 wt% in the protolith to almost 40 wt% in ultracataclasites, whereas MgO decreases from ~22 wt% to <16 wt% in the ultracataclasites (Table 1).

In relation to the trace elements, it was observed from protolith to fault rocks an enrichment in Rb, V, Ni, Zr, but overall in Zn and Pb (Fig. 5e, Table 2). The enrichment factors (EF), which are based on Al normalization ($X_{EF} = [(X/Al)_{sample}/(X/Al)_{PAAS}]$ where X is an specific trace element and PAAS, the post-Archean average shale compositions of Taylor and McLennan, 1985), were calculated for these trace elements. In practical terms, EFs > 3 represent a detectable enrichment of an element over average crustal concentrations, and EFs > 10 represent
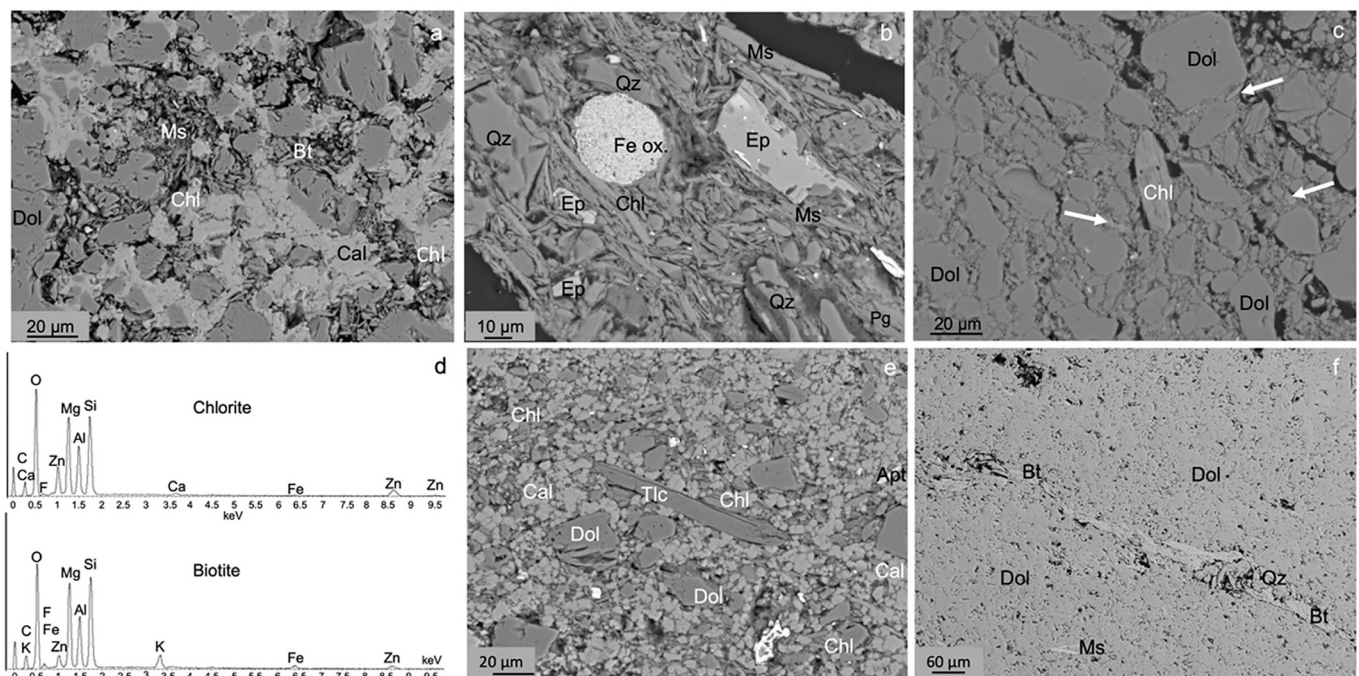

Fig. 3. BSE images and EDX spectra showing texture and chemical features of the fault rocks: a-b) Details of the fine-grained matrix of ultraclasites showing the presence of silicates in addition to carbonates; c) aspect of the matrix of a cataclasite, including dolomite clasts of different micrometer sizes and chlorite laths (in the center and the white arrows); d) EDX spectra of chlorite and biotite with Zn; e) fault rock matrix including also a talc grain among chlorites and carbonates; f) view of the protolith, a dolostone. Mineral abbreviations according to Whitney and Evans (2010), Bt, biotite; Cal, calcite; Chl, chlorite; Dol, dolomite; Ep, epidote; Fe ox., Fe oxide; Ms, muscovite; Qz, quartz; Pg, paragonite; Tlc, talc.
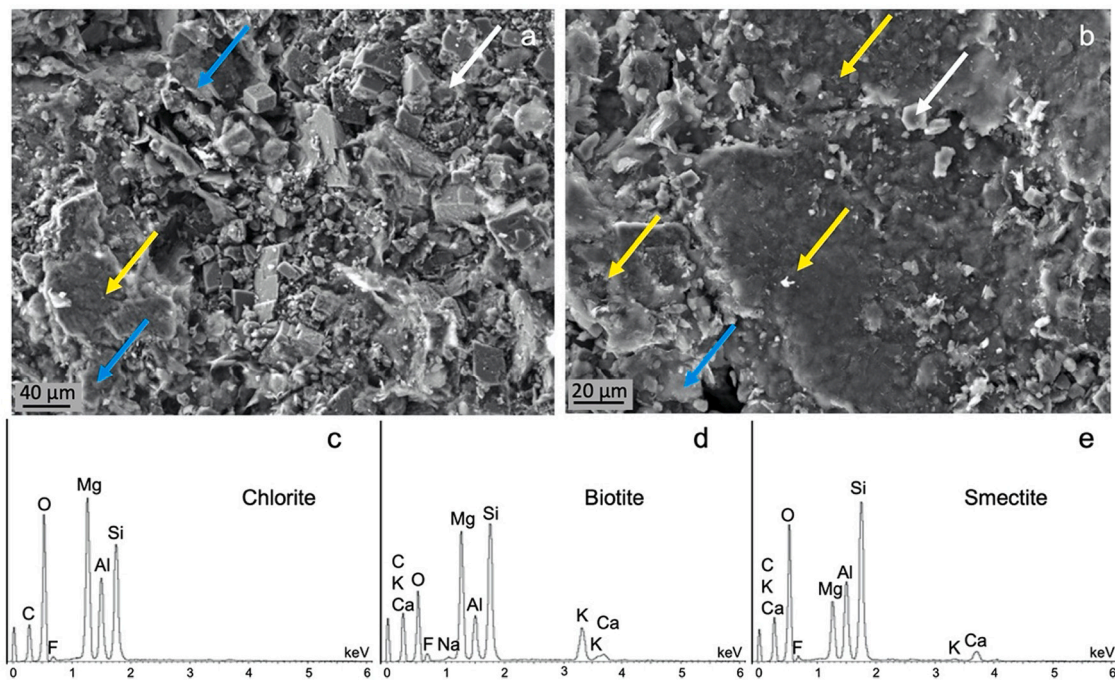
Fig. 4. a-b) SE images corresponding to the fault plane; c-e) EDX spectra of chlorite, biotite and smectite detected in this location. Yellow arrows for chlorite grains, white arrows for biotite crystals and blue arrows for smectite. (For interpretation of the references to colour in this figure legend, the reader is referred to the web version of this article.)

a moderate to strong degree of enrichment (Algeo and Tribovillard, 2009). EFs are >10 in Zn and Pb for most of the fault rocks, which is considered a moderate to strong degree of enrichment, relative to their average crustal abundance. There is also a significant REE enrichment of the ultracataclasites, and this increase is as well progressive from the host rock to the samples in the fault plane (Fig. 5f).

XRF mapping reveals irregular bands enriched in Si, Al, Fe, Ti and Zn along the predominantly carbonate matrix of the fault rocks and surrounding the dolomite clasts (Fig. 6). This enrichment is also visible towards the fault plane, in the reddish and yellowish zone of the ultrafine-grained matrix of the ultracataclasites.

4.3. Chemistry of trioctahedral phyllosilicates

Trioctahedral phyllosilicates, mainly chlorites and biotites from fault rocks were analysed in detail using the EPMA and the TEM to ascertain in their origin and genetic relationship in the framework of the fault dynamic.

The structural formula of biotites show Zn contents between 0.25 and 0.5 apfu. The Si content is usually lower than 2.8 apfu (Fig. 7a and Table A in supplementary material). In relation to the sum of interlayer cations, this is between 0.62 and 0.37 apfu (Fig. 7b). There is only one biotite analysis that fits with their theoretical composition and it is close to the phlogopite end-member (Fig. 7a-b).

The composition of chlorite from the cataclasites is Mg-rich (clinochlore variety), although with a highly variable content of Mg (3.49–4.83 apfu) and Si (2.88–3.33 apfu) (Fig. 7c). Fe is generally low ($\leq$ 0.11 apfu) and also Ti ($<$ 0.05 apfu), while there is variability of Zn values, from nil up to 0.91 apfu (Fig. 7d, Table B and C in supplementary material). The sum of interlayer cations (K + Ca) ranges between 0.05 and 0.20 apfu. The analyses with Si values <2.95 apfu corresponds to the ones with no Zn or < 0.10 apfu, which are the richest in Mg. The sum of octahedral cations is usually <6 apfu and exhibits a negative correlation with the Si content. By contrast, the Mg-rich chlorites located on the fault plane (Fig. 4a-b) show a more homogeneous chemistry, with narrower ranges for Si, Mg and Al. These chlorites have almost no Zn and

Fe, which are always $\leq$0.03 apfu and Ti is totally absent (Fig. 7c-d). The interlayer content of these chlorites, due to trace amounts of Ca and K, are always <0.05 apfu. Some of the smectitic domains located on the fault planes show Al-rich dioctahedral beidellite-like composition and others close to a Mg saponite (Table D in supplementary material). The scarcity and smallness of the biotite grains on the fault plane prevented the obtention of EPMA analyses.

In relation to the talc, the chemistry of this mineral is the typical Mg-rich composition, with very small quantities of Al (<0.15 apfu) distributed between the tetrahedral and octahedral sheets and no Fe at all.

4.4. Chlorite thermometry

Semi-empirical thermometry was applied in chlorite-bearing samples corresponding to the fault plane. The chlorite analyses were selected according to the criteria related to the sum of interlayer cations and the value of octahedral vacancies given by Bourdelle et al. (2013) and Inoue et al. (2018). The temperature estimations for the two thermometers are rather similar, with differences that do not exceed 25 °C. The average temperature obtained for the chlorites located on the fault plane is 179 °C according to the Bourdelle et al. (2013) thermometer and 191 °C according to the Inoue et al. (2018) thermometry proposal (Table 3). There is a wide range of temperatures (from 110 °C to 280 °C) although as it can be observed in Fig. 7e the predominant values are around 140–220 °C. In relation to the chlorites from the cataclasites, the sum of interlayer cations (<0.20 apfu, but high for the thermometry requirements) and/or the presence of Zn, whose possible effect on the geothermometry is unknown, and hence a possible source of error on the temperature determination, prevented reliable temperature estimations.

4.5. TEM characterization

Based on XRD and SEM data two fault rocks were chosen to ascertain in the genetic relationship between biotites and chlorites and a third sample was prepared to attempt determination of the paragenesis of talc.
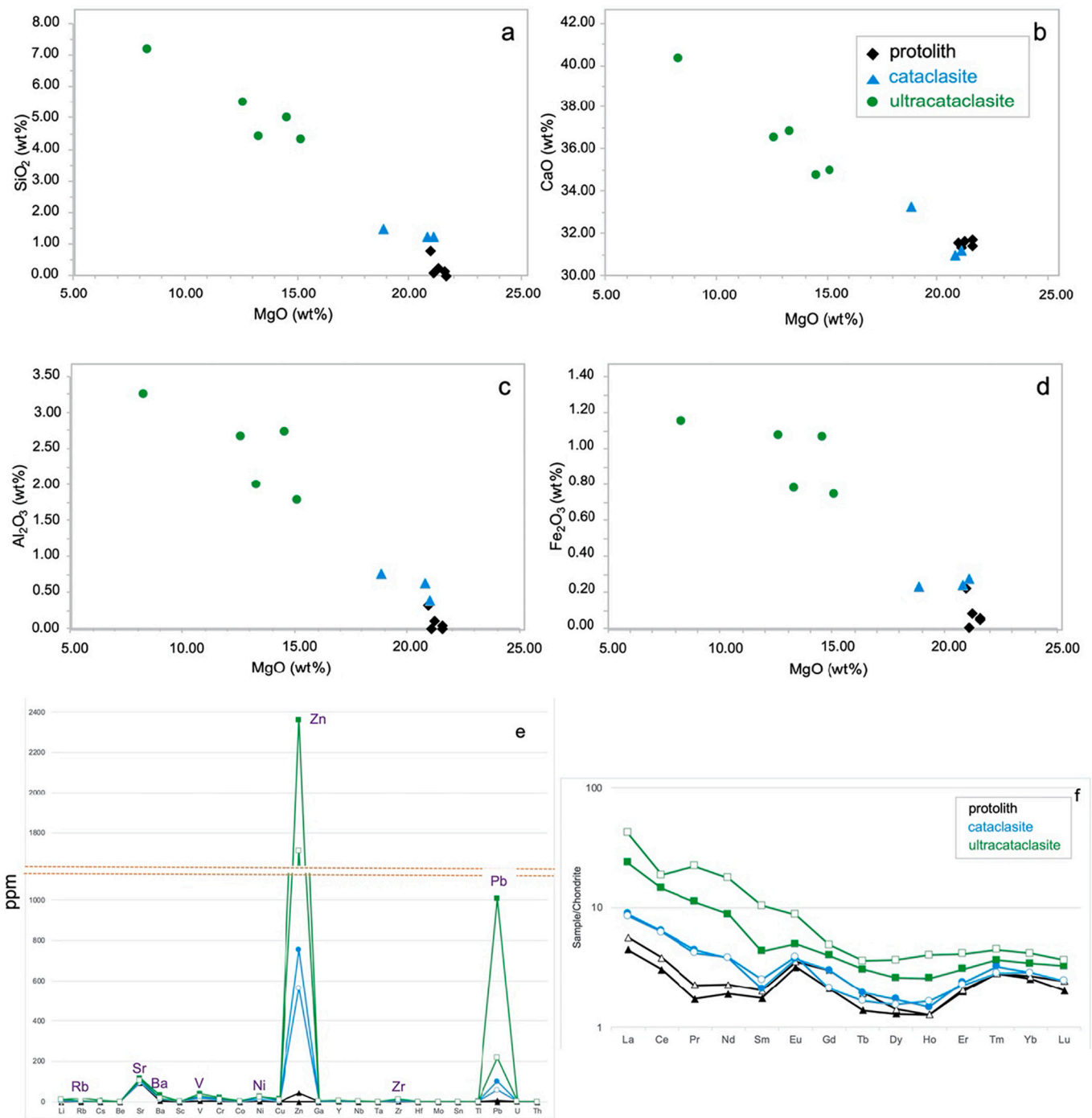
Fig. 5. Major element binary diagrams based on X-ray fluorescence data showing chemical differences and trace elements plots based on the chemical bulk composition of the studied rocks (protolith and fault rocks): a) MgO vs SiO₂; b) MgO vs CaO; c) MgO vs Al₂O₃; d) MgO vs Fe₂O₃; e) trace elements-pattern; f) chondrite normalized REE-patterns. For trace elements, two samples from each type of rock where selected (overall data in Table 2).

At TEM scale, biotite was detected with lattice fringes of 10 Å and 1 M polytype and also chlorite packets with the characteristic 14 Å periodicity. In addition, other phyllosilicates such as muscovite, illitic mica and kaolinite were detected at nanoscale. The detailed study of some biotitic grains showed the presence of individual 14 Å layers in the lattice fringe images. In these packets it is easy to observe defects as bending and layer terminations that in some cases are terminations of one or two layers of biotite by a layer of chlorite (Fig. 8a). The strain contrast, due to internal deformation of the crystalline structure, originated by the difference of size of the two kinds of layers, is apparently associated with these defects. But the most significant feature was the

identification of packets which include lattice fringes of 10 Å and 14 Å, sometimes alternating individual layers (24 Å) and sometimes forming packets of several layers of 10 Å alternating with several layers of 14 Å (Fig. 8b-c). The X-ray maps showed that in the crystal where these lattice fringe images were taken there are bands richer in K than others (Fig. 9a). The rich ones correspond to biotitic mica, although the content in K is around 0.5 apfu, the same chemical feature previously described for the biotites analysed by EPMA. The bands with low K content (~ 0.20 apfu) correspond to Mg chlorite with a sum of octahedral cations ~5.50 apfu. The particular chemistry of biotites and chlorites agrees with the observations done in the lattice fringe images, where the presence of

Table 1

Whole-rock analyses of major elements of Padul Fault samples (oxide wt%, XRF).

Samples	SiO$_2$	Al$_2$O$_3$	Fe$_2$O$_3$	MgO	CaO	K$_2$O	Na$_2$O	MnO	TiO$_2$	P$_2$O$_5$	LOI	Total
Protolith												
FP8	0.00	0.00	0.05	21.62	31.73	0.00	0.00	0.00	0.04	0.00	46.00	99.44
Dol pro	0.14	0.05	0.06	21.59	31.40	0.03	0.00	0.00	0.05	0.00	46.28	99.60
FP-7	0.80	0.32	0.22	20.96	31.53	0.11	0.00	0.00	0.06	0.01	45.64	99.65
JU4	0.13	0.00	0.00	21.08	31.34	< LLD	< LLD	< LLD	0.04	< LLD	46.85	99.44
JU1n	0.26	0.11	0.08	21.27	31.63	0.03	< LLD	< LLD	0.04	< LLD	46.06	99.48
Cataclasites												
FP-2	1.27	0.63	0.24	20.80	30.96	0.05	< LLD	< LLD	0.08	0.01	45.52	99.56
FP-9	1.26	0.40	0.27	21.07	31.21	0.27	< LLD	< LLD	0.06	0.01	45.29	99.84
JU1b	1.52	0.76	0.23	18.85	33.27	0.12	< LLD	< LLD	0.05	0.01	45.15	99.96
Ultracataclasites												
FP-1	5.04	2.73	1.06	14.55	34.79	0.28	0.08	< LLD	0.12	0.03	41.36	100.04
MO1	5.50	2.67	1.07	12.60	36.56	0.16	0.04	0.01	0.15	0.03	40.72	99.51
JU6b	4.31	1.78	0.74	15.15	34.97	0.10	0.06	0.01	0.09	0.03	42.67	99.91
JU6d	4.43	2.00	0.78	13.31	36.81	0.12	0.06	0.01	0.12	0.03	41.86	99.53
JU5b	7.19	3.26	1.15	8.32	40.34	0.06	0.18	< LLD	0.16	0.03	38.84	99.53

Table 2

Trace elements (ppm, ICP-MS) of Padul Fault samples.

	Protolith					Cataclasites			Ultracataclasites				
Samples	**FP8**	**Dol pro**	FP-7	JU4	**JU1n**	**FP-2**	FP-9	**JU1b**	**FP-1**	MO1	JU6b	**JU6d**	JU5b
Li	0	0.54	2.13	0	1.02	3.32	5.23	5.7	10.24	15.43	11.56	11.31	12.79
Rb	0.37	1.28	2.8	0.29	1.3	2.32	5.91	4.82	18.25	11.03	5.23	5.44	2.95
Cs	0.08	0.14	0.28	0.08	0.18	0.98	0.73	1.23	6.13	3.74	2.61	2.29	1.8
Be	0.05	0.06	0.05	0.05	0.07	0.13	0.03	0.17	0.46	0.49	0.4	0.36	0.63
Sr	94.23	113.59	99.85	92.6	105.09	113.26	240.68	94.86	116.37	101.8	102.39	107.15	59.19
Ba	5.35	6.76	14.95	5.11	6.64	15.81	22.28	12.15	32.28	21.26	19.4	17.13	14.8
Sc	0	0	0	0	0	0.33	0.24	0.38	2.03	2.18	1.25	1.65	2.49
V	5.6	4.99	7.94	7.46	7.09	18.08	6.75	16.29	39.45	40.55	32.52	27.46	34.65
Cr	3.32	3.65	7.96	7.58	4.71	9.43	7.84	7.15	20.51	18.94	11.26	12.77	16.4
Co	0.03	0.33	0.62	0	0.1	0.68	0.33	0.57	2.77	2.86	2.22	2.45	2.81
Ni	4.31	3.51	7.92	4.23	4.43	12.82	6.9	11.59	26.55	18.92	26.62	24.83	45.36
Cu	1.61	0	1.81	1.26	2.17	2.12	2.16	2.94	14.64	5.92	6.26	8.17	14.67
Zn	45.01	0.85	23.56	9.74	35.35	755.93	55.58	564.22	2364.3	1222.2	2144	1708.8	5122.4
Ga	0	0.05	0.48	0	0.13	0.86	0.62	0.93	3.31	3.33	2.13	2.62	4.31
Y	1.22	1.49	2.48	1.14	1.45	1.89	1.91	2	3.85	3.72	4.06	6.07	4.84
Nb	0.96	1	0.92	0.96	1.08	1.24	0.96	1.49	2.68	3	2.35	2.54	3.18
Ta	0.02	0	0.09	0.02	0.02	0.16	0.03	0.05	0.26	0.21	0.12	0.21	0.19
Zr	1.25	1.55	1.27	1.31	1.94	3.2	1.53	4.84	13.13	16.14	10.88	10.81	16.37
Hf	0	0	0	0	0	0	0	0	0.29	0.37	0.11	0.1	0.25
Mo	0.77	1.21	0.33	0.12	0.54	0.37	0.25	0.55	0.85	0.78	1.14	1.03	1.04
Sn	0	0	0	0	0	0	0	0	0.21	0.18	0	0	0
Tl	0.04	0.17	0.05	0.03	0.18	0.38	0.1	0.57	1.84	1.32	0.66	0.88	0.67
Pb	8.06	0	23.88	1.93	6.5	100.32	21.68	58.84	1006.9	441.46	322.38	218.46	431.86
U	1.39	1.21	1.17	0.56	1.54	1.52	0.65	1.68	2.06	2.83	2.55	1.63	1.27
Th	0	0	0	0	0	0	0	0	1.07	1.58	0.73	0.87	1.28
La	1.06	1.34	1.99	1.04	1.39	2.1	2.04	2.01	5.58	5.61	5.09	9.84	6.85
Ce	1.87	2.34	4.22	1.82	2.54	3.91	3.5	3.83	8.85	11.3	7.22	11.36	10.44
Pr	0.16	0.21	0.46	0.15	0.24	0.41	0.41	0.39	1.03	1.24	0.97	2.05	1.39
Nd	0.87	1.04	2.04	0.82	1.15	1.74	1.76	1.75	4.02	4.89	3.97	8	5.51
Sm	0.26	0.3	0.44	0.3	0.3	0.31	0.32	0.37	0.64	0.89	0.71	1.53	1.03
Eu	0.18	0.2	0.27	0.18	0.2	0.21	0.22	0.22	0.28	0.33	0.31	0.49	0.37
Gd	0.42	0.6	0.597	0.39	0.43	0.597	0.597	0.42	0.796	1	0.33	0.97	0.62
Tb	0.05	0.07	0.1	0.05	0.05	0.07	0.1	0.06	0.11	0.14	0.04	0.13	0.07
Dy	0.32	0.35	0.59	0.31	0.33	0.42	0.47	0.38	0.64	0.71	0.44	0.9	0.63
Ho	0.07	0.07	0.12	0.06	0.07	0.08	0.12	0.09	0.14	0.15	0.15	0.22	0.18
Er	0.32	0.33	0.41	0.31	0.33	0.38	0.38	0.36	0.49	0.51	0.51	0.66	0.58
Tm	0.07	0.07	0.08	0.07	0.07	0.08	0.08	0.07	0.09	0.09	0.09	0.11	0.1
Yb	0.41	0.43	0.48	0.41	0.43	0.46	0.46	0.46	0.55	0.58	0.54	0.67	0.62
Lu	0.05	0.06	0.07	0.05	0.06	0.06	0.06	0.06	0.08	0.08	0.07	0.09	0.09

Note: In bold samples used for the Fig. 5.

chlorite layers inside biotites would be responsible of the lower K content than that which might be expected for the micas.

With respect to Zn, in the chlorite packets reaches values up to 1.30 apfu. Specifically, in some zones which include also the presence of muscovite laths and kaolinite coexisting with the carbonates and biotite (Fig. 9b), it was observed that in the EDX map of Zn there are bright thin bands next to biotite packets that correspond to chlorite bands (Fig. 9c). The negative correlation of this map with the EDX map of the K allows to observe a very subtle banding in the K content just in the zones in which Zn-bearing chlorite is present alternating with biotite (Fig. 9d). The Mg
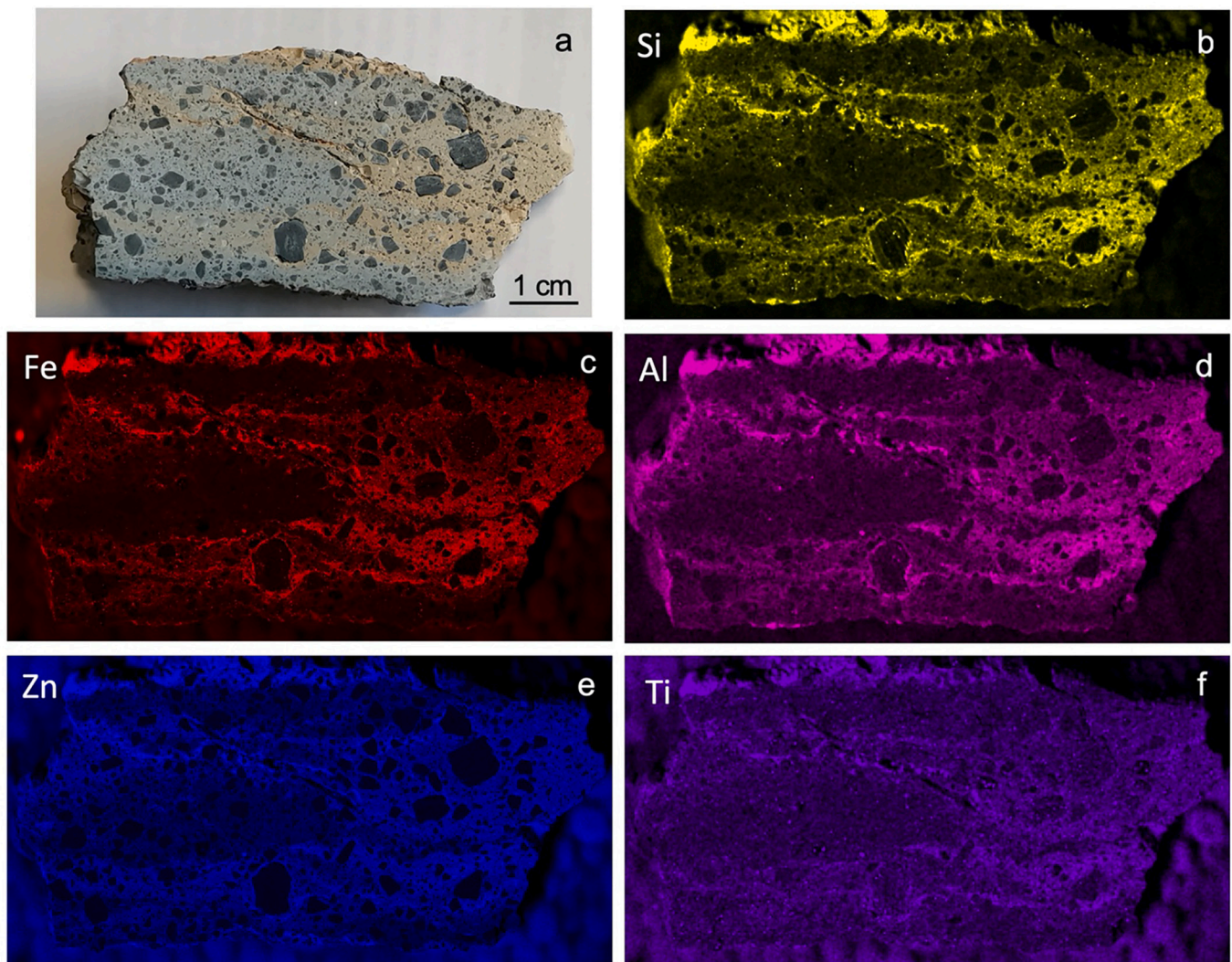
Fig. 6. X-ray microfluorescence compositional maps of Si, Al, Fe, Ti and Zn corresponding to a cataclasite.

and Al EDX maps permit the clear identification of the muscovite and biotite packets in the right upper corner and the kaolinite packet in the middle of the images (Fig. 9e-f). The STEM-EDX spectra of chlorite and biotite corresponding to the positions indicated in Fig. 9c confirm that whereas the Mg-chlorite has Zn, this element was not detected in the biotites (Fig. 9g-h). The detailed characterization of some chlorite grains shows that in some cases they are Zn free, but when the Zn is present, the distribution is not homogeneous inside them either because it shows an increase from one part to another (Fig. 10a-c) or because it oscillates perpendicular to the elongation of the grains (Fig. 10d-e).

In relation to the presence of talc in these samples, although it is rare (Fig. 3e), the identification of this phase by XRD (< 2 μm fraction) in one of the samples from the fault plane was significant enough to try to characterize it at the nanoscale as it was not possible at the micrometer scale. The textural images and the EDX maps show the predominance of carbonate clasts (dolomite and calcite) and the minor presence of phyllosilicates as biotite and talc as well as xenomorph quartz crystals. These minerals are normally observed alone, occupying gaps among the carbonates (Fig. 11a-b). The size of the talc grains is always less than several micrometers which explains the difficulty in locating them in the SEM. Most of talc grains are around 0.5 μm long and 100 nm thick and, although they are very small, the lattice fringe images and electron diffractions show defect-free crystals (Fig. 11c-d). The textural location of the talc, as it is observed in Fig. 11, always follows the same pattern, that is, between both types of carbonates.

5. Discussion

5.1. Fault rock composition and clay genesis

The intense cataclasis during the fault activity would increase the permeability of the surrounding rock mass facilitating the fluids circulation in the fault zone, which would act as a domain driving mobilised fluids from deep source and promoting fluid-rock interaction processes that led to clay neoformation. To clarify these points, we determined the mineral assemblages corresponding to the host rocks and the fault rocks and detected the enrichment and/or depletion in some elements (major and trace) from the protolith to the damaged rock and the distribution of these elements in the fault rocks. In addition, the presence of chlorite has allowed the application of recent methods of chlorite thermometry.

The XRF analyses are useful to determine fluid-related alterations. In our case, as well as the clear increase observed in SiO_2, Al_2O_3, Fe_2O_3 and CaO (Fig. 5a-d) from the protolith to the ultracataclasites, the μXRF has shown that these elements and also Ti and Zn draw irregular bands along the predominantly carbonate matrix of the rocks, surrounding the dolomite clasts (Fig. 6). This textural aspect of the fault rocks points to a relation with a fluid circulation episode which had to promote the chemical element variations and the authigenesis of quartz and phyllosilicate grains. The significant presence of Zn (> 1200 ppm in the ultracataclasites, Table 2), a trace element with a higher solubility in hydrothermal systems than in other environments as for instance, the
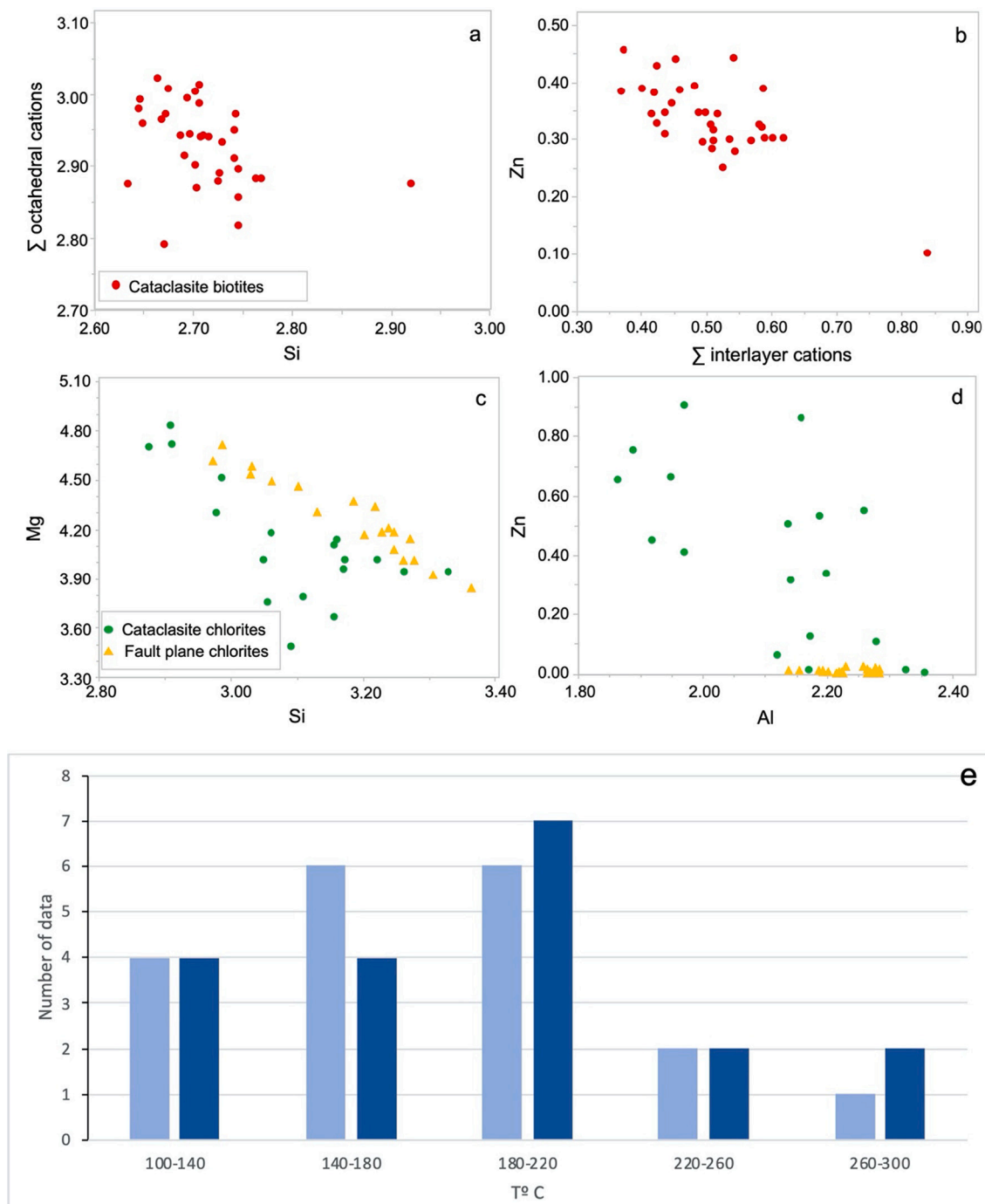
Fig. 7. Diagrams showing the chemical composition of biotites (a-b) and chlorites (c-d) and histogram (e) showing the geothermometric data obtained from the chemical analyses of the chlorites located on the fault plane of the Padul Fault (navy blue: Inoue geothermometer, light blue: Bourdelle geothermometer). (For interpretation of the references to colour in this figure legend, the reader is referred to the web version of this article.)

Table 3
Summary of temperatures calculated in chlorites with semi-empirical methods.

Geothermometer	Range (°C)	Average (°C)	n
Bourdelle et al., 2013	118–276	179 ± 41	20
Inoue et al., 2018	107–278	191 ± 48	

Note: Errors are expressed at SD level and n is numbers of analyses.

metamorphic environment (London et al., 1988) is consistent with these observations. As a matter of fact, hydrothermal fluids play a significant role in the genesis of a variety of Zn-rich clay minerals present in Zn mineral deposits (Buatier et al., 2016; Balassone et al., 2020 and references therein). In relation to the probable source of the Zn (and Pb), mineral deposits of F-Pb-Zn, some of them mined, are frequent in the Triassic carbonate sequence of the Alpujárride Complex (Martín et al., 1987 and references therein). They are strata-bound, mainly stratiform, hence they must have a sedimentary origin linked to diagenetic processes of lagoonal fine-grained dolomites.

Whereas the protolith, which is essentially a low-grade metamorphic dolostone is made of dolomite and minor quantities of quartz and micas (biotite and muscovite), the fault rocks show also calcite, mainly in the ultracataclasites, minor presence of Fe, Ti oxides and apatite and
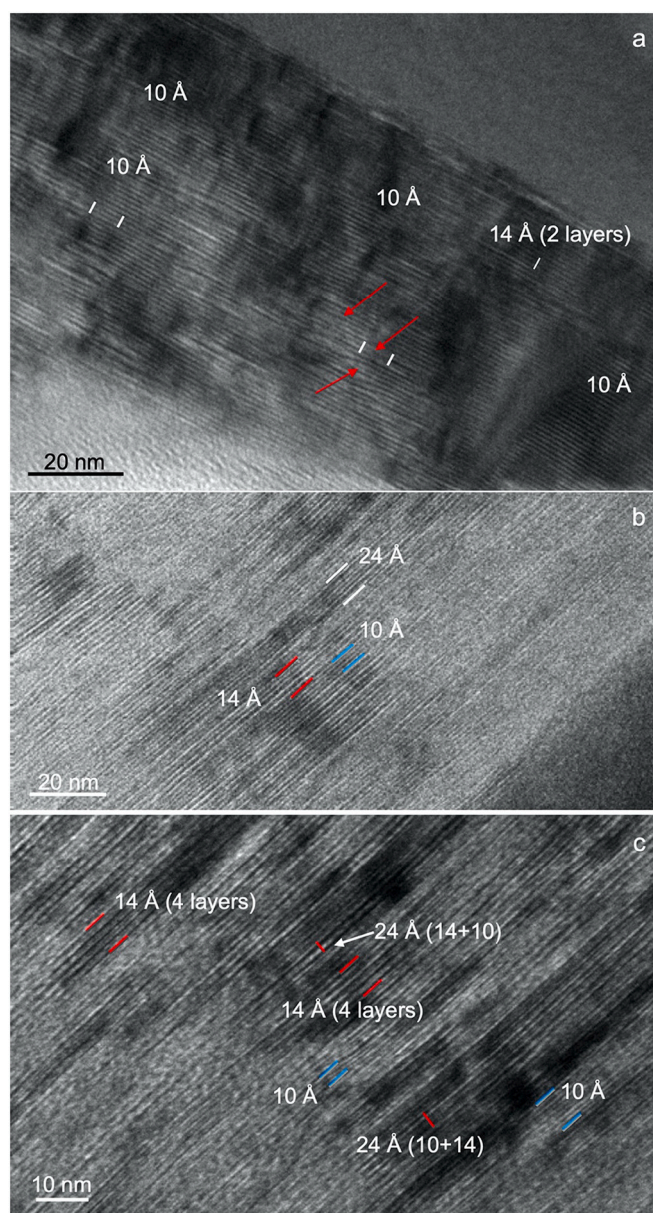
Fig. 8. HRTEM images showing the presence in the same packet lattice fringes of different values: a) biotite which includes individual 14 Å layers.; b and c) thin packets of 24 Å, 14 Å and 10 Å periodicity. Layers terminations are indicated by red arrows. (For interpretation of the references to colour in this figure legend, the reader is referred to the web version of this article.)

phyllosilicates such as illitic micas, kaolinite, chlorite, smectite and sporadic talc as well as muscovite and biotite in both ultra- and cataclasites. It is obvious that the protolith has undergone a certain enrichment in silicates in the fault area.

The detailed characterization of the chlorites as well as the talc, present uniquely in the fault rocks, has allowed to determine that they are Mg-rich chlorites, but also that Zn, with an EF > 10 in the fault rocks, is preferentially partitioned in them. Nevertheless, not all analysed chlorites include Zn in their composition. Specifically, chlorites from the fault plane have no Zn, at all (Fig. 7d). The same observation with respect to the Zn was done for the biotites, although in this case they are also present in the protolith but without Zn. In fact, the presence of the biotites decreases from protolith to the fault plane, the opposite that occurs with the chlorites. According to Feng et al. (2022) the Zn variation in chlorites of hydrothermal origin is likely caused by fluid compositional difference. In addition to the variable presence of Zn in the trioctahedral phyllosilicates (biotites and chlorites) of the cataclasites, the particular composition of these micas with abnormally low K contents, relative to a theoretical biotite, points to at least a partial alteration of them in the fault rocks. The nanoscale characterization of these trioctahedral phyllosilicates in cataclasites, where it was observed that biotitic packets include 14 Å layers (Fig. 8a) and packets with 3–6 layers of 10 Å alternating with packets of several layers of 14 Å or 24 Å (Fig. 8b-c) indicate a layer-by-layer transformation from parent biotite to chlorite product. The parallel orientation of the (001) layers corresponding to both phases suggests a topotactic replacement of biotite by chlorite facilitated by the structural and chemical similarities. This kind of transformation has been previously described in low-grade metamorphic contexts (Jiang and Peacor, 1994; Barrenechea et al., 2000) and also in hydrothermal systems (Jiménez-Millán et al., 2008; Airaghi et al., 2020). Nevertheless, the chlorites identified on the fault plane (Fig. 4), which are parallel to the fracture surface, have a more homogeneous composition (Fig. 7) and show bigger sizes than chlorites from cataclasites. In this case, it seems more appropriate to consider a dissolution-crystallization mechanism, which would affect the host rocks.

The analyses of chlorites from the fault plane and the application of chlorite thermometry (Bourdelle et al., 2013; Inoue et al., 2018) points to a temperature for chlorites on the fault plane close to 200 °C. These temperatures are typical for pervasive hydrothermal fluids that could circulate along the fault plane but also migrating laterally through the permeable carbonate formations soaking the surroundings (cataclasites) and promoting changes in the geochemistry and mineralogy, more evident in the fault plane that at certain distance, also due to the temperature which would be higher along the main fault planes contributing to dissolution processes.

The presence of other trioctahedral phyllosilicate, talc, was detected by SEM in cataclasites and more significantly by XRD and TEM in samples taken from the fault plane and composed essentially by dolomite and calcite. The small size of the talc grains observed at nanoscale (< 0.5 µm), which do not form aggregates and are always located among both carbonates suggest a genesis from dolomite promoted by the activity of silica-rich hydrothermal fluids in a low-temperature environment. According to the experimental study of Wan et al. (2017), talc can form from the interaction of $CaMg(CO_3)_2$, SiO_2 and H_2O at temperatures as low as ≤ 200 °C and low PCO_2, but increasing the reaction rate with increasing temperature and always above 100 °C. This reaction has even been documented within faults and shear zones (e.g., Hecht et al., 1999; Viti and Collettini, 2009) in the range of 170–400 °C at 1–2 kbar depending on the CO_2 content and it is one of the most cited origins of talc deposits (Tornos and Spiro, 2000; Chatir et al., 2022 and references therein). The reaction implies the generation of CO_2 and calcite as by-products as well as talc (Gordon and Greenwood, 1970):

$$3CaMg(CO_3)_2 + 4SiO_2 + H_2O \rightarrow Mg_3(Si_4O_{10})(OH)_2 + 3CaCO_3 + 3CO_2$$
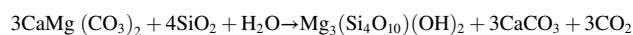
These conditions are consistent with the chlorite thermometry.

To sum up, the presence of fault-controlled hydrothermal fluids promoted geochemical changes and mineral reactions in the fault rocks as the direct talc and chlorite precipitation from circulating fluids in the fault plane at temperatures close to 200 °C and the layer-by-layer transformation from parent biotite to chlorite product in the cataclasites, according to chlorite data and electron microscopy observations. The presence of smectite in the fault plane and the fault rocks together with kaolinite and illite could be the result of the circulation of late fluids, may be related to the final step of the hydrothermal activity in the fault, the same as for much of the calcite whose presence is remarkable in the ultracataclasites. Calcite mineralization as cement or filling veins implies the closing of fluid pathways and a reduction of the permeability of the fault rocks.
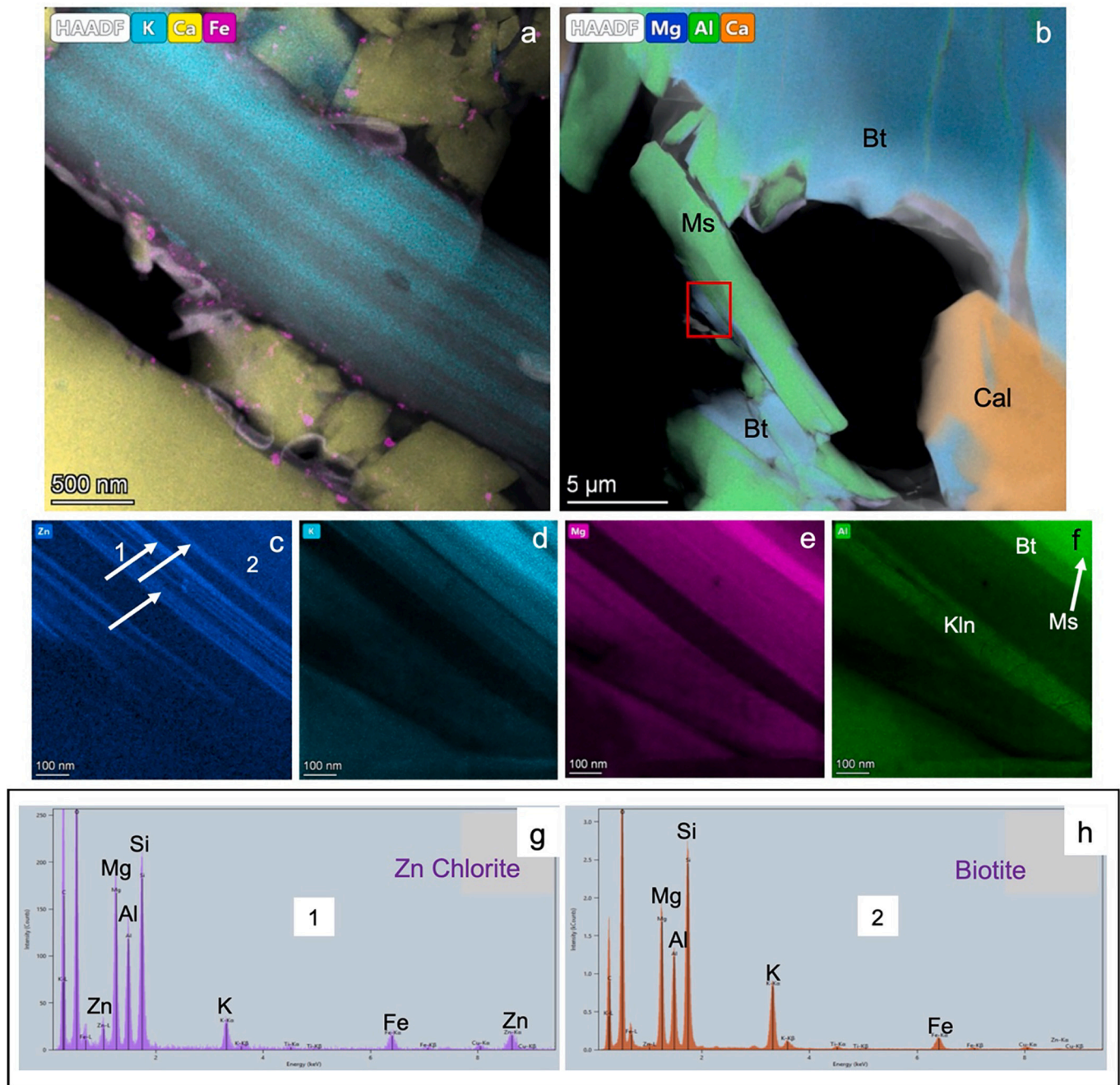
Fig. 9. a) K vs Ca vs Fe STEM-EDX map of site of interest reported in Fig. 8; b) Mg vs Al vs Ca STEM-EDX map with a red rectangle indicating the position of the STEM-EDX maps on the right (c-f). Below, g) STEM-EDX spectra of Zn chlorite (white arrows in c) and h) biotite whose location is indicated in the Zn EDX map. Cal, calcite; Kln, kaolinite; Ms., muscovite; Bt, biotite. (For interpretation of the references to colour in this figure legend, the reader is referred to the web version of this article.)

5.2. The potential role of clay minerals on the Padul Fault behavior

According to several authors (Schleicher et al., 2010; Van der Pluijm, 2011), the presence of newly grown clay minerals, can be a key factor in the behavior of active fault systems. Smeraglia et al. (2017) stated that phyllosilicates can facilitate aseismic creep by dissipation of elastic strain energy, more clearly if these minerals are located in ultrathin layers, even for quantities ≤3 wt%, as it was experimentally tested. Here we have described chlorite and smectite preferentially oriented, parallel to the fault plane. Smectitic clays are among the weakest materials in the crust, with extremely low friction coefficients ($\mu < 0.23$) when compared with illite and chlorite ($\mu = 0.27$–0.32) (Ikari et al., 2009). In

addition, other authigenic clay, talc, is considered the softest known natural mineral and one of the few minerals capable of absolute fault weakening, as it has a friction coefficient between ~0.05 and 0.23, depending on the temperature, pressure, fluid conditions, and applied strain rate (Escartín et al., 2008; Moore and Lockner, 2008). In our case, talc is present in very minor amounts, which generates doubts about its possible influence in the fault behavior. In any case, whereas in the cataclasites the talc grains detected are several tens of micrometers long, in the fault plane however they are normally <0.5 μm long and < 100 nm width (Fig. 11). According to Collettini et al. (2009a) this difference in the size could be a consequence of interlayer delaminations of talc grains which would provoke a grain size reduction providing in turn a
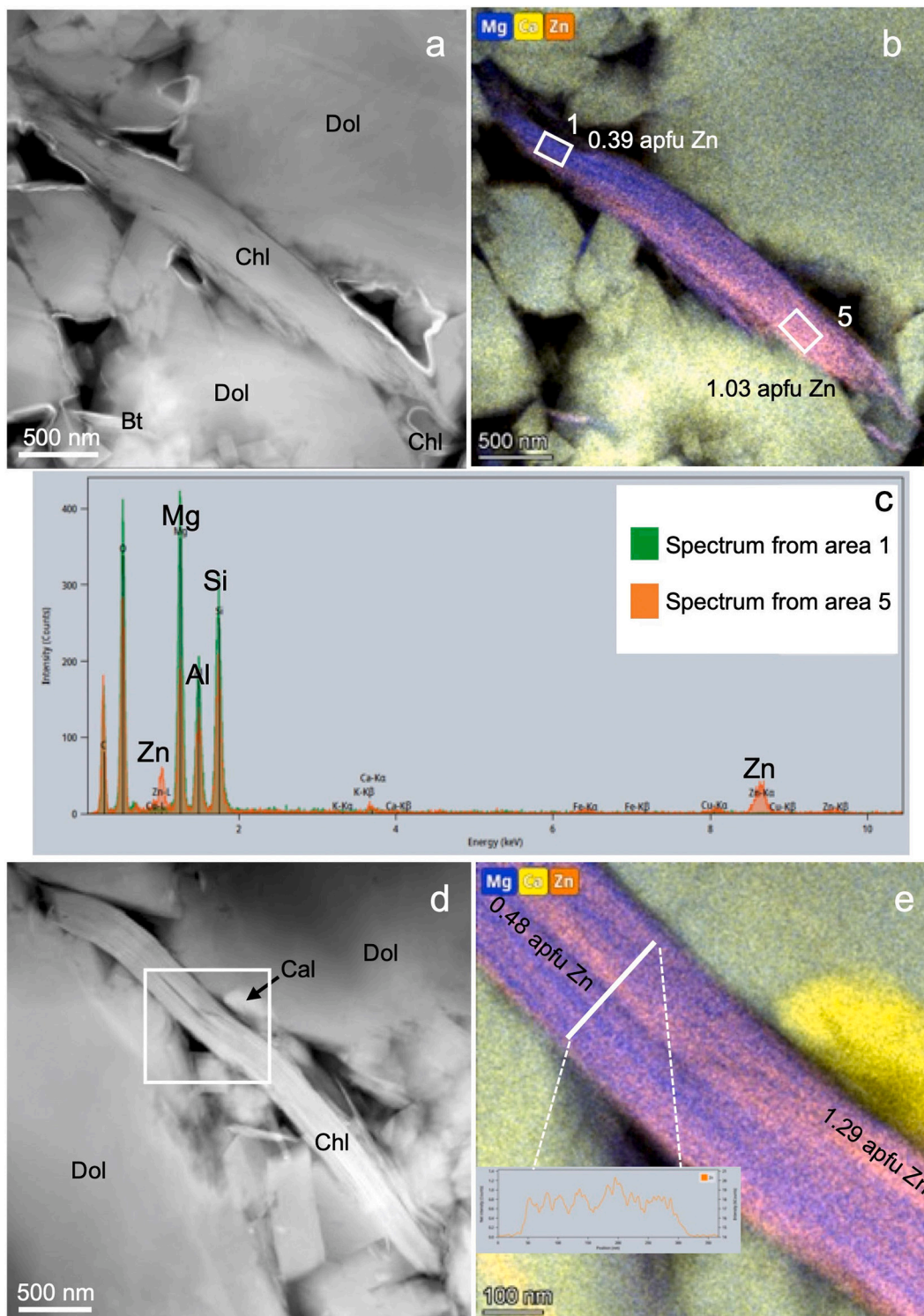
Fig. 10. a) HAADF image showing the mineral distribution in an area with a chlorite crystal; b) Mg vs Ca vs Zn STEM-EDX map of this area with location of the chlorite analyses showing the extreme Zn compositions; c) two overlapped energy-dispersive X-ray (EDX) spectra corresponding to the chlorite packet of previous images (a-b) with clear differences in the content of Mg and Zn; d) HAADF image with location of next STEM-EDX map; e) Mg vs Ca vs Zn STEM-EDX map of an area of a chlorite where the Zn content changes across the width of the elongated crystal as it is shown by the colors and the inset (Zn profile).

number of possible frictional sliding surfaces. But even so, these talc grains do not form an interconnected framework in the Padul samples as described by Collettini et al. (2009a) and fault weakening depends strongly on rock fabric and the distribution of weak phases within a fault zone (Collettini et al., 2009b).

The Padul Fault is the most relevant and best exposed active normal fault of the central Betics (Betic Cordillera, Spain). But the absence of instrumental or historical seismic events suggests that the fault is now unlocked and that its activity occurs, at least partially, by creep, reducing the possibility of large seismogenic events. According to the GPS data and an average fault dip of 55°, the average displacement on the fault surface should be of around 0.78 mm/yr (Gil et al., 2017) which
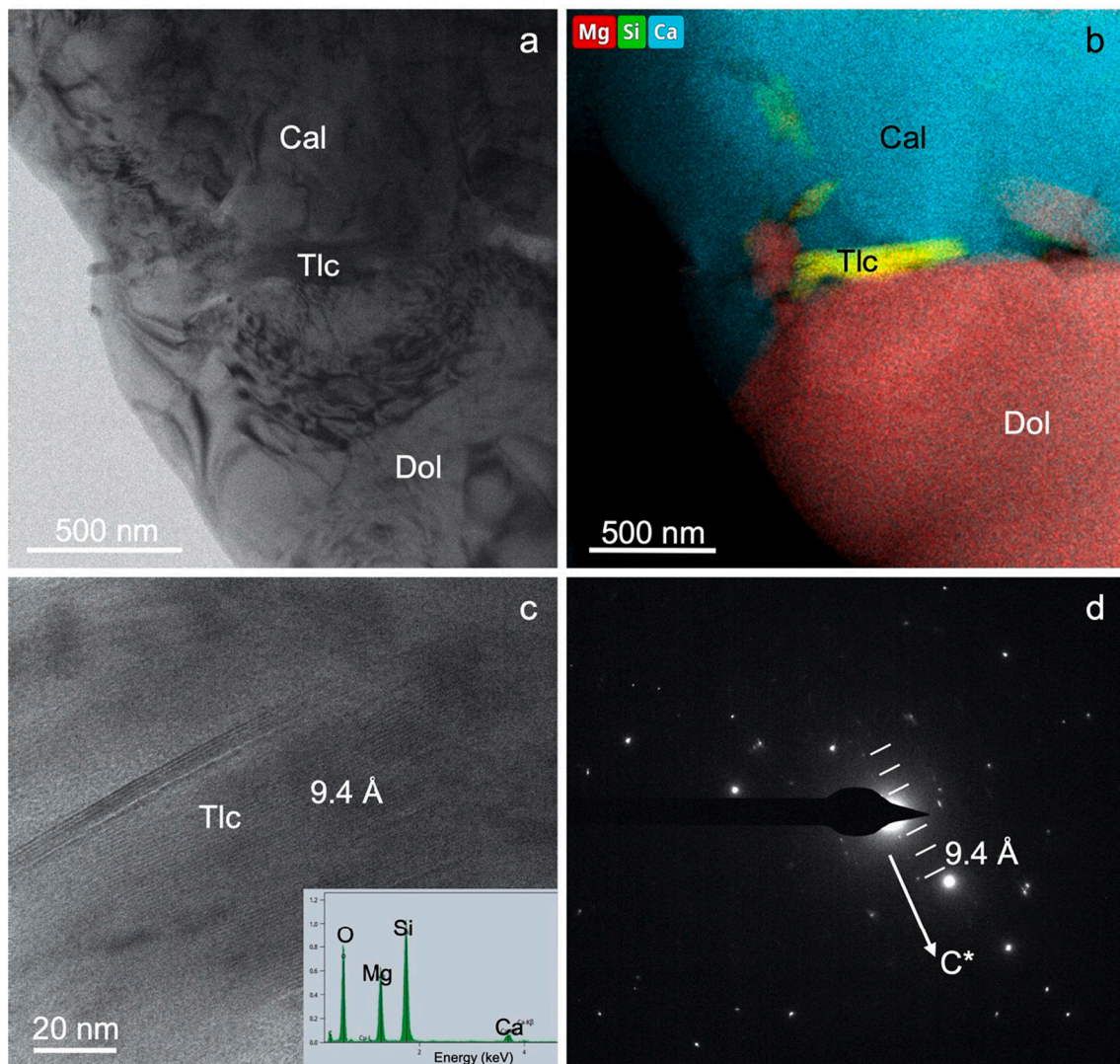
Fig. 11. a and b) textural and Mg vs Si vs Ca STEM-EDX map showing the mineral association based on dolomite (Dol), calcite (Cal) and talc between them (Tlc); c) lattice fringe image of the talc grain with the 9.4 Å basal *d*-value characteristic of this phyllosilicate and EDX spectrum; d) selected area electron diffraction pattern showing 00*l* reflections of talc.

is a bit higher rate than the one based on stratigraphic markers (0.16 to 0.35 mm/yr, Sanz de Galdeano et al., 2012). In conclusion, Gil et al. (2017) considered that Padul Fault probably has an important part of aseismic deformation, although more data covering a broader time than the last 500 years would be necessary to quantify the percentages of aseismic and seismic deformation of this active fault. Particularly, the identification of soft-sediment structures produced by liquefaction in the Quaternary sediments next to Padul Fault (< 1 km) was attributed to seismic shocks of a moderate-high-magnitude, although not necessarily produced by an earthquake associate with this fault (Alfaro et al., 2001). In this context, the fault rocks characterization from the chemical and mineralogical point of view, with the identification of authigenic clay minerals as a consequence of fluid-rock interaction processes, displays results consistent with the geodetic data from Gil et al. (2017). It has been demonstrated that newly grown clay minerals can promote weakening mechanisms at shallow crustal levels that contribute to the creep over the seismic stick-slip and reduce the possibility of large seismogenic events (Wintsch et al., 1995; Smeraglia et al., 2017).

6. Conclusions

Clay minerals not detected in the protolith of the Padul Fault were described in the fault rocks. Among them, chlorite is the most significant both in fault rocks and directly on the fault plane. Both the presence of Zn in chlorites and the chemistry of biotites from the cataclasites and the textural relationship of both minerals up to the nanoscale suggest a layer-by-layer transformation. Nevertheless, chlorites from the fault plane have no Zn and show more homogeneous compositions. The chlorite thermometry indicates temperatures between 140 and 220 °C. Talc grains were also detected among carbonates. These data together with the geochemical features, Si, Al, Fe, Ca, Ti and Zn enrichment towards the ultracataclasites in form of irregular bands, points to the presence of fault-controlled hydrothermal fluids promoting geochemical changes and mineral reactions in the fault rocks, as the precipitation of chlorite and talc from fluids at temperatures close to 200 °C. The identification of authigenic clay minerals as a consequence of fluid-rock interaction processes are results consistent with the geodetic data and the absence of instrumental or historical seismic events in the Padul Fault that points to a predominant fault activity by creep.

and RNM-179 of the Junta de Andalucía.

Credit author statement

I.A. and M.R. conducted field observations and sampling. I.A. and F. N. interpreted the X-ray diffractograms. I.A and M. R. worked and interpreted the whole-rock chemical analyses. I.A., J.J.M. and F.N. performed microscopic observations (SEM and TEM, mineralogical, textural, and chemical analyses). All the authors discussed the analytical results and prepared the manuscript.

Declaration of Competing Interest

The authors declare that they have no known competing financial interests or personal relationships that could have appeared to influence the work reported in this paper.

Data availability

Data will be made available on request.

Acknowledgements

Appendix A. Supplementary data

Supplementary data to this article can be found online at https://doi.org/10.1016/j.clay.2022.106669.

References

Abad, I., Jiménez-Millán, J., Schleicher, A.M., van der Pluijm, B., 2017. Mineral characterization, clay quantification and Ar-Ar dating of faulted schists in the Carboneras and Palomares Faults (Betic Cordillera, SE Spain). Eur. J. Mineral. 29, 18–34. https://doi.org/10.1127/ejm/2017/0029-2580.

Abad, I., Jiménez-Millán, J., Sánchez-Roa, C., Nieto, F., Velilla, N., 2019. Neo-crystallization of clay minerals in the Alhama de Murcia Fault (SE Spain): implications for fault mechanics. Clay Miner. 54, 1–13. https://doi.org/10.1180/clm.2019.2.

Airaghi, L., Dubacq, B., Verlaguet, A., Bourdelle, F., Bellahsen, N., Gloter, A., 2020. From static alteration to mylonitization: a nano- to micrometric study of chloritization in granitoids with implications for equilibrium and percolation length scales. Contrib. Mineral. Petrol. 175, 108. https://doi.org/10.1007/s00410-020-01749-2.

Aldaya, F., García-Dueñas, V., Navarro-Vila, F., 1979. Los Mantos Alpujárrides del tercio central de las Cordilleras Béticas. Ensayo de correlación tectónica de los Alpujárrides. Acta Geol. Hisp. 14, 154–166.

Alfaro, P., Galindo-Zaldivar, J., Jabaloy, A., López-Garrido, A.C., Sanz de Galdeano, C., 2001. Evidence for the activity and paleoseismicity of the Padul fault (Betic Cordillera, southern Spain). Acta Geol. Hisp. 36, 283–295.

Algeo, T.J., Tribovillard, N., 2009. Environmental analysis of paleoceanographic systems based on molybdenum–uranium covariation. Chem. Geol. 268, 211–225. https://doi.org/10.1016/j.chemgeo.2009.09.001.

Alonso-Chaves, F.M., Orozco, M., 1998. El sistema de fallas extensionales en La Axarquía (Sierras de Tejeda y La Almijara, Cordilleras Béticas). Geogaceta 24, 15–18.

Azañón, J.M., Crespo-Blanc, A., 2000. Exhumation during a continental collision inferred from the tectonometamorphic evolution of the Alpujárride complex in the central Betics (Alborán Domain, SE Spain). Tectonics 19, 549–565. https://doi.org/10.1029/2000tc900005.

Azañón, J.M., Goffé, B., 1997. Ferro- and magnesiocarpholite assemblages as record of high-P, low-T metamorphism in the Central Alpujarrides, Betic Cordillera (SE Spain). Eur. J. Mineral. 9, 1035–1051. https://doi.org/10.1127/ejm/9/5/1035.

Azañón, J.M., García-Dueñas, V., Martínez Martínez, J.M., Crespo Blanc, A., 1994. Alpujárride tectonic sheets in the central Betics and similar Eastern allochthonous units (SE Spain). Compt. Rendus Acad. Sci. Paris 318, 667–674.

Balassone, G., Scognamiglio, V., Nieto, F., Mondillo, N., Boni, M., Cappelletti, P., Arfè, G., 2020. The nature of Zn-phyllosilicates in the nonsulfide Mina Grande and Cristal zinc deposits (Bongará District, Northern Peru): the TEM-HRTEM and AEM perspective. Am. Mineral. 105, 1223–1241.

Barrenechea, J.F., Rodas, M., Frey, M., Alonso-Azcarate, J., Mas, J.R., 2000. Chlorite, corrensite, and chlorite-mica in late Jurassic fluvio-lacustrine sediments of the Cameros basin of northeastern Spain. Clay Clay Miner. 48, 256–265.

Bourdelle, F., Parra, T., Chopin, C., Beyssac, O., 2013. A new chlorite geothermometer for diagenetic to low-grade metamorphic conditions. Contrib. Mineral. Petrol. 165, 723–735. https://doi.org/10.1007/s00410-012-0832-7.

Braga, J.M., Martín, J.M., 1987. Sedimentación cíclica lagunar y bioconstrucciones asociadas en el Trías Superior alpujárride. Cuadernos de Geología Ibérica 11, 459–473.

Buatier, M.D., Chauvet, A., Kanitpanyacharoen, W., Wenk, H.R., Ritz, J.F., Jolivet, M., 2012. Origin and behavior of clay minerals in the Bogd fault gouge, Mongolia. J. Struct. Geol. 34, 77–90.

Buatier, M., Choulet, F., Petit, S., Chassagnon, R., Vennemann, T., 2016. Nature and origin of natural Zn clay minerals from the Bou Arhous Zn ore deposit: evidence from electron microscopy (SEM-TEM) and stable isotope compositions (H and O). Appl. Clay Sci. 132, 377–390.

Chatir, A., Berger, J., Ennih, N., Triantafyllou, A., de Parseval, P., Errami, E., Diot, H., Baele, J.-M., Aghzer, A.M., Monnier, C., Boutaleb, M., 2022. Formation of the Nkob talc deposit by contact metamorphism and fluid infiltration into siliceous dolostones (Moroccan Anti-Atlas). Ore Geol. Rev. 140.

Collettini, C., Viti, C., Smith, S.A.F., Holdsworth, R.E., 2009a. The development of interconnected talc networks and weakening of continental low-angle normal faults. Geology 37, 567–570. https://doi.org/10.1130/G25645A.1.

Collettini, C., Niemeijer, A., Viti, C., Marone, C., 2009b. Fault zone fabric and fault weakness. Nature 462, 907–910. https://doi.org/10.1038/nature08585.

Delgado, F., Estévez, A., Martín, J.M., Martín Algarra, A., 1981. Observaciones sobre la estratigrafía de la formación carbonatada de los mantos alpujárrides (Cordilleras Béticas). Estud. Geol. 37, 45–57.

Escartín, J., Andreani, M., Hirth, G., Evans, B., 2008. Relationships between the microstructural evolution and the rheology of talc at elevated pressures and temperatures. Earth Planet. Sci. Lett. 268, 463–475. https://doi.org/10.1016/j.epsl.2008.02.004.

Faulkner, D.R., Lewis, A.C., Rutter, E.H., 2003. On the internal structure and mechanics of large strike-slip fault zones: field observations of the Carboneras fault in southeastern Spain. Tectonophysics 367, 235–251.

Feng, Y., Chu, G., Xiao, B., Li, R., Deng, C., Li, G., Shi, H., 2022. Chlorite mineralogy, geochemistry and exploration implications: a case study of the Xiaokelehe porphyry Cu-Mo deposit in NE China. Ore Geol. Rev. 140, 104568 https://doi.org/10.1016/j.oregeorev.2021.104568.

Galindo Zaldívar, J., Jabaloy, A., Serrano, I., Morales, J., González-Lodeiro, F., 1999. Recent and present-day stresses in the Granada Basin (Betic Cordilleras): example of a late Miocene-present-day extensional basin in a convergent plate boundary. Tectonics 18, 686–702.

Galindo-Zaldívar, J., Gil, A.J., Borque, M.J., González-Lodeiro, F., Jabaloy, A., Marín-Lechado, C., Ruano, P., Sanz de Galdeano, C., 2003. Active faulting in the internal zones of the central Betic Cordilleras (SE, Spain). J. Geodyn. 36, 239–250.

Gil, A.J., Galindo-Zaldívar, J., Sanz de Galdeano, C., Borque, M.J., Sánchez-Alzola, A., Martínez-Martos, M., Alfaro, P., 2017. The Padul normal fault activity constrained by GPS data: Brittle extension orthogonal to folding in the central Betic Cordillera. Tectonophysics 712-713, 64–71. https://doi.org/10.1016/j.tecto.2017.05.008.

Gordon, T.M., Greenwood, H.J., 1970. The reaction dolomite + quartz + water = talc + calcite + carbon dioxide. Am. J. Sci. 268, 225–242.

Hecht, L., Freiberger, R., Gilg, H.A., Grundmann, G., Kostitsyn, Y.A., 1999. Rare earth element and isotope (C, O, Sr) characteristics of hydrothermal carbonates: genetic implications for dolomite-hosted talc mineralization at Gopfersgrun (Fichtelgebirge, Germany). Chem. Geol. 155, 115–130.

Hürtgen, J., Rudelsdorf, A., Grützner, C., Reicherter, K., 2013. Morphotectonics of the Padul-Nigüelas Fault Zone, southern Spain. Ann. Geophys. 56, S0679. https://doi.org/10.4401/ag-6208.

Ikari, M.J., Saffer, D.M., Marone, C., 2009. Frictional and hydrologic properties of clay-rich fault gouge. J. Geophys. Res. 114, B05409. https://doi.org/10.1029/2008JB006089.

Inoue, A., Inoué, S., Utada, M., 2018. Application of chlorite thermometry to estimation of formation temperature and redox conditions. Clay Miner. 53, 143–158.

Jiang, W., Peacor, D.R., 1994. Formation of corrensite, chlorite and chlorite-mica stacks by replacement of detrital biotite in low-grade pelitic rocks. J. Metamorph. Geol. 12, 867–884.

Jiménez-Millán, J., Abad, I., Nieto, F., 2008. Contrasting alteration processes in hydrothermal altered dolerites from the Betic Cordillera (Spain). Clay Miner. 43, 267–280.

Jiménez-Millán, J., Abad, I., Hernández-Puentes, P., Jiménez-Espinosa, R., 2015. Influence of phyllosilicates and fluid-rock interaction on the deformation style and mechanical behaviour of quartz-rich rocks in the Carboneras and Palomares fault areas (SE Spain). Clay Miner. 50, 619–638.

Johnson, C., 1997. Resolving denudational histories in orogenic belts with apatite fission-track thermochronology and structural data: an example from southern Spain. Geology 25, 623–626.

Kristensen, M.B., Childs, C., Olesen, N.O., Korstgard, J.A., 2013. The microstructure and internal architecture of shear bands in sand-clay sequences. J. Struct. Geol. 46, 129–141.

London, D., Hervig, R.L., Morgan, G.B., 1988. Melt-vapor solubilities and elemental partitioning in peraluminous granite-pegmatite systems: experimental results with Macusani glass at 200 MPa. Contrib. Mineral. Petrol. 99, 360–373.

Martín, J.M., Torres-Ruiz, J., Fonboté, L., 1987. Facies control of strata-bound ore deposits in carbonate rocks: the F-(Pb-Zn) deposits in the Alpine Triassic of the Alpujárrides, southern Spain. Mineral. Deposita 22, 216–226.

Montenat, C., Ott D'Estevou, P., 1995. Late Neogene basins evolving in the Eastern Betic transcurrent fault zone: An illustrated review. In: Friend, P.F., Dabrio, C.J. (Eds.), Tertiary Basins of Spain. Cambridge University Press, Cambridge, pp. 372–386.

Moore, D.E., Lockner, D.A., 2008. Talc friction in the temperature range 25°–400 °C: Relevance for fault-zone weakening. Tectonophysics 449, 120–132. https://doi.org/10.1016/j.tecto.2007.11.039.

Pouchou, J.L., Pichoir, F., 1985. "PAP" (f) (r) (t) procedure for improved quantitative microanalisis. In: Armstrong, J.T. (Ed.), Microbeam Analysis. San Francisco Press, San Francisco, pp. 104–106.

Santanach, P., Sanz de Galdeano, C., Bousquet, J.C., 1980. Neotectónica de las regiones mediterráneas de España (Cataluña y Cordilleras Béticas). Bol. Inst. Geol. Min. Esp. 91-92, 417–440.

Sanz de Galdeano, C., 1976. Datos sobre las deformaciones neógenas y cuaternarias del sector del Padul. Reunión sobre la geodinámica de la Cordillera Bética y Mar de Alborán. Universidad de Granada.

Sanz de Galdeano, C., 1990. Estructura y estratigrafía de la Sierra de los Guajares y sectores próximos (Conjunto Alpujárride, Cordilleras Béticas). Estud. Geol. 46, 123–134.

Sanz de Galdeano, C., 2022. La Cordillera Bética. Editorial Punto Rojo Libros, Sevilla.

Sanz de Galdeano, C., Alfaro, P., 2004. Tectonic significance of the present relief of the Betic Cordillera. Geomorphology 63, 175–190.

Sanz de Galdeano, C., López-Garrido, A.C., 1999. Estratigrafía y estructura de las unidades alpujárrides en el borde occidental de Sierra Nevada (Granada, España). Rev. Soc. Geol. Esp. 12, 187–198.

Sanz de Galdeano, C., López-Garrido, A.C., 2003. Revisión de las Unidades Alpujárrides de las Sierras de Tejeda, Almijara y Guájares (Sector Central de la Zone Interna Bética, Provincias de Granada y Málaga). Rev. Soc. Geol. Esp. 16, 135–149.

Sanz de Galdeano, C., López-Garrido, A.C., 2014. Structure of the Sierra de Lujar (Alpujarride complex, Betic Cordillera). Estud. Geol. 70, e005.

Sanz de Galdeano, C., Estévez, A., López-Garrido, A.C., Rodríguez-Fernández, J., 1984. La fracturación tardía al SW de Sierra Nevada (Terminación occidental del Corredor de la Alpujarra). Estud. Geol. 40, 183–191.

Sanz de Galdeano, C., García-Tortosa, F.J., Peláez, J.A., Alfaro, P., Azañón, J.M., Galindo- Zaldívar, J., López-Casado, C., López-Garrido, A.C., Rodríguez-

Fernández, J., Ruano, P., 2012. Main active faults in the Granada and Guadix-Baza Basins (Betic Cordillera). J. Iber. Geol. 38, 209–223. https://doi.org/10.5209/rev_jige.2012.v38.n1.39215.

Sanz de Galdeano, C., Prieto-Mera, J., Andreo, B., 2019. Structure of the Alpujarride complex and hydrogeological observations to the NW of Sierra Tejeda (Granada and Malaga provinces, Betic Internal Zone, Spain). Estud. Geol. 75, e090 https://doi.org/10.3989/egeol.43395.509.

Schleicher, A.M., van der Pluijm, B.A., Warr, L.N., 2010. Nanocoatings of clay and creep of the San Andreas fault at Parkfield, California. Geology 38, 667–670.

Simancas, J.F., Campos, J., 1993. Compresión NNW-SSE tardi a postmetamórfica, y extensión subordinada, en el Complejo Alpujárride (Dominio de Alborán, Orógeno Bético). Rev. Soc. Geol. Esp. 6, 23–35.

Smeraglia, L., Billi, A., Carminati, E., Cavallo, A., Di Toro, G., Spagnuolo, E., Zorzi, F., 2017. Ultra-thin clay layers facilitate seismic slip in carbonate faults. Sci. Rep. 7, 664.

Taylor, S.R., McLennan, S.M., 1985. The Continental Crust: Its Composition and Evolution. Blackwell, Oxford.

Tesei, T., Collettini, C., Barchi, M.R., Carpenter, B.M., Di Stefano, G., 2014. Heterogenous strength and fault zone complexity of carbonate-bearing thrusts with possible implications for seismicity. Earth Planet. Sci. Lett. 408, 307–318.

Tornos, F., Spiro, B.F., 2000. The geology and isotope geochemistry of the talc deposits of Puebla de Lillo (Cantabrian zone, northern Spain). Econ. Geol. 95, 1277–1296. https://doi.org/10.2113/95.6.1277.

Van der Pluijm, B., 2011. Natural fault lubricants. Nat. Geosci. 4, 217–218.

Verdecchia, S., Collo, G., Zandomeni, P.S., Wunderlin, C., Fehrmann, M., 2019. Crystallochemical indexes and geothermobarometric calculations as a multiproxy approach to P-T condition of the low-grade metamorphism: the case of the San Luis Formation, Eastern Sierras Pampeanas of Argentina. Lithos 324-325, 385–401. https://doi.org/10.1016/j.lithos.2018.11.021.

Viti, C., Collettini, C., 2009. Growth and deformation mechanisms of talc along a natural fault: a micro/nanostructural investigation. Contrib. Mineral. Petrol. 158, 529–542.

Wan, Y., Wang, X., Chou, I., Hu, W., Zhang, Y., Wang, X., 2017. An experimental study of the formation of talc through interaction at 100-200°C and vapor-saturation pressures. Geofluids 3942826. https://doi.org/10.1155/2017/3942826.

Whitney, D.L., Evans, B.W., 2010. Abbreviations for names of rock-forming minerals. Am. Mineral. 95, 185–187.

Wintsch, R.P., Christoffersen, R., Kronenberg, A.K., 1995. Fluid-rock reaction weakening of fault zones. J. Geophys. Res. Solid Earth 100, 13021–13032.